

Local observation of plasmon focusing in Talbot carpets

Sudhir Cherukulappurath,¹ Dominique Heinis,¹ Jean Cesario,^{1,2} Niek. F. van Hulst,^{1,3} Stefan Enoch,² and Romain Quidant^{1,3*}

¹ ICFO-Institut de Ciències Fòniques, Mediterranean Technology Park, 08860 Castelldefels (Barcelona), Spain.

² Institut Fresnel, UMR CNRS 6133, Université Paul Cézanne Aix-Marseille III, 13397 Marseille Cedex 20, France

³ ICREA-Institució Catalana de Recerca i Estudis Avançats, 08010 Barcelona, Spain

*romain.quidant@icfo.es

Abstract: We present a detailed experimental and theoretical study of plasmon Talbot effect. A theoretical model based on simple scattering theory is developed to describe the Talbot self-imaging pattern generated by a linear arrangement of cylindrical nanostructures forming a periodic array. We first show the experimental observation of plasmon Talbot carpets created by propagating surface plasmon polaritons (SPP) interacting with cylindrical nanostructures positioned on a thin Au film using leakage radiation microscopy. Such images provide information on the distribution of the plasmon intensity close to the nanostructures. Next, heterodyne interferometer based near-field imaging is carried out to extract information on the plasmonic modes forming the Talbot carpet deployment. We report the experimental observation of Talbot focal spots with dimensions down to $\lambda/4$.

©2009 Optical Society of America

OCIS codes: (070.6760) Talbot effect; (240.6680) Surface plasmons; (250.5403) Plasmonics.

References and links

1. W. L. Barnes, A. Dereux, and T. W. Ebbesen, "Surface plasmon subwavelength optics," *Nature* **424**(6950), 824–830 (2003).
2. H. Raether, "Surface Plasmons on Smooth and Rough Surfaces and on Gratings", Vol. 111 of Springer Tracts in Modern Physics (Springer-Verlag, Berlin, 1988).
3. F. J. Garcia de Abajo, "Light Scattering by particle and hole arrays," *Rev. Mod. Phys.* **79**(4), 1267–1290 (2007).
4. A. G. Curto, and F. Javier Garcia de Abajo, "Near-Field Optical Phase Antennas for Long-Range Plasmon Coupling," *Nano Lett.* **8**(8), 2479–2484 (2008).
5. S. I. Bozhevolnyi, and F. A. Pudonin, "Two-Dimensional Micro-Optics of Surface Plasmons," *Phys. Rev. Lett.* **78**(14), 2823–2826 (1997).
6. H. Ditlbacher, J. R. Krenn, G. Schider, A. Leitner, and F. R. Aussenegg, "Two-dimensional optics with surface plasmon polaritons," *Appl. Phys. Lett.* **81**(10), 1762–1764 (2002).
7. J.-C. Weeber, Y. Lacroute, A. Dereux, E. Devaux, T. Ebbesen, C. Girard, M. U. Gonzalez, and A.-L. Baudrion, "Near-field characterization of Bragg mirrors engraved in surface plasmon waveguides," *Phys. Rev. B* **70**(23), 235406 (2004).
8. A. Drezet, A. L. Stepanov, H. Ditlbacher, A. Hohenau, B. Steinberger, F. R. Aussenegg, A. Leitner, and J. R. Krenn, "Surface plasmon propagation in an elliptical corral," *Appl. Phys. Lett.* **86**(7), 74104 (2005).
9. M. U. Gonzalez, J.-C. Weeber, A.-L. Baudrion, A. Dereux, A. L. Stepanov, J. R. Krenn, E. Devaux, and T. W. Ebbesen, "Design, near-field characterization, and modeling of 45 surface-plasmon Bragg mirrors," *Phys. Rev. B* **73**(15), 155416 (2006).
10. A. Hohenau, J. R. Krenn, A. L. Stepanov, A. Drezet, H. Ditlbacher, B. Steinberger, A. Leitner, and F. R. Aussenegg, "Dielectric optical elements for surface plasmons," *Opt. Lett.* **30**(8), 893–895 (2005).
11. F. M. Huang, T. S. Kao, V. A. Fedotov, Y. Chen, and N. I. Zheludev, "Nanohole Array as a lens," *Nano Lett.* **8**(8), 2469–2472 (2008).
12. H. F. Talbot, "Facts relating to optical science, No. IV," *Philos. Mag.* **9**, 401–407 (1836).
13. M. V. Berry, and S. Klein, "Integer, fractional and fractal Talbot effects," *J. Mod. Opt.* **43**, 2139–2164 (1996).
14. A. W. Lohmann, and D. E. Silva, "An interferometer based on the Talbot effect," *Opt. Commun.* **2**(9), 413–415 (1971).
15. A. W. Lohmann, "An array illuminator based on the Talbot effect," *Optik (Stuttg.)* **79**, 41–45 (1988).

16. M. Testorf, J. Jahns, N. A. Khilo, and A. M. Goncharenko, "Talbot effect for oblique angle of light propagation," *Opt. Commun.* **129**(3-4), 167–172 (1996).
17. F. M. Huang, N. Zheludev, Y. Chen, and F. J. Garcia de Abajo, "Focusing of light by a nanohole array," *Appl. Phys. Lett.* **90**(9), 091119 (2007).
18. M. R. Dennis, N. I. Zheludev, and F. J. Garcia de Abajo, "The plasmon Talbot effect," *Opt. Express* **15**(15), 9692–9700 (2007).
19. A. A. Maradudin, and T. A. Leskova, "The Talbot effect for a surface Plasmon polariton," *N. J. Phys.* **11**(3), 033004 (2009).
20. W. Zhang, C. Zhao, J. Wang, and J. Zhang, "An experimental study of the plasmonic Talbot effect," *Opt. Express* **17**(22), 19757 (2009).
21. A. Archambault, T. V. Teperik, F. Marquier, and J. J. Greffet, "Surface plasmon Fourier optics," *Phys. Rev. B* **79**(19), 195414 (2009).
22. J. Cesario, M. U. Gonzalez, S. Cheylan, W. L. Barnes, S. Enoch, and R. Quidant, "Coupling localized and extended plasmons to improve the light extraction through metal films," *Opt. Express* **15**(17), 10533–10539 (2007).
23. A. L. Stepanov, J. R. Krenn, H. Ditlbacher, A. Hohenau, A. Drezet, B. Steinberger, A. Leitner, and F. R. Aussenegg, "Quantitative analysis of surface plasmon interaction with silver nanoparticles," *Opt. Lett.* **30**(12), 1524 (2005).
24. A. Drezet, A. Hohenau, A. L. Stepanov, H. Ditlbacher, B. Steinberger, N. Galler, F. R. Aussenegg, A. Leitner, and J. R. Krenn, "How to erase surface plasmon fringes," *Appl. Phys. Lett.* **89**(9), 091117 (2006).
25. J. W. Goodman, "Introduction to Fourier Optics", 3rd Ed., Robert & Com., 2005.
26. M. L. M. Balistreri, J. P. Korterik, L. Kuipers, and N. F. van Hulst, "Phase Mapping of Optical Fields in Integrated Optical Waveguide Structures," *J. Lightwave Technol.* **19**(8), 1169–1176 (2001).
27. M. L. M. Balistreri, J. P. Korterik, L. Kuipers, N. F. van Hulst, "Local Observations of Phase Singularities in Optical Fields in Waveguide Structures," *Phys. Rev. Lett.* **85**(2), 294–297 (2000).
28. H. L. Offerhaus, B. van den Bergen, M. Escalante, F. B. Segerink, J. P. Korterik, and N. F. van Hulst, "Creating Focused Plasmons by Non-collinear Phase-matching on Functional Gratings," *Nano Lett.* **5**(11), 2144–2148 (2005).

1. Introduction

In recent years the study and manipulation of subwavelength optical fields is attracting great interest owing to the potential applications in biophotonics, ultrafast communication and quantum optics. In particular, the field of surface plasmon optics has opened new avenues in understanding the light-matter interaction at the nanoscopic level [1]. Surface plasmon polaritons (SPP) are two-dimensional electron waves propagating along a metal-dielectric interface coupled to the electromagnetic fields that are evanescent in the direction perpendicular to the surface [2]. The surface confinement of SPPs make them interesting candidates for studying several optical phenomena as the propagation properties of SPPs are strongly dictated by the surface morphology of the interface between the metal and the dielectric. Any surface defect at the interface can act as a scattering center thereby altering the propagation of the SPPs. The interaction of SPPs with surface defects has been studied extensively both theoretically [3, 4] as well as experimentally [5]. The sensitivity of SPP towards surface defects has led researchers to make use of the property for designing several optical elements like Bragg mirrors [6–9], beam splitters, interferometers [7] and nanolenses [10, 11].

The scattering of SPP with periodically patterned defects is of particular interest as it invokes several interesting phenomena that are analogous to those found in conventional optics. One such effect is the revival or self-imaging of the field after transmission or reflection from a periodic structure, called Talbot effect [12]. This effect, originally discovered by H. F. Talbot, has been observed in classical as well as in quantum optics. The Talbot length τ , at which the periodicity is revived, is given by $\tau = 2a^2 / \lambda$ in the paraxial approximation, where a is the period of the array and λ the wavelength. The self-imaging Talbot effect can be regarded as the interference of different orders of the electromagnetic waves that are diffracted when they pass through a periodic structure.

The Talbot effect in optics is well studied both theoretically as well as experimentally [13–16]. F. M. Huang *et al.* have reported on the free space Talbot effect after transmission through a quasi-crystal array of nano-holes on a metallic film [17]. Sub-wavelength light

spots were observed for different heights from the nano-hole array plane. However, studies of the Talbot effect on electromagnetic surface waves have mostly been restricted to theoretical simulations. Dennis *et al.* has shown theoretically that it is possible to create complex plasmon carpets containing hot spots by a row of periodically spaced surface defects on a metal surface [18]. Their system consisted of a row of holes drilled in Ag film, illuminated from the backside. Both numerical and analytical calculations for plasmonic Talbot effect were discussed and the revival of propagating plasmons at the Talbot distances was observed. More recently, Maradudin and Leskova have reported some theoretical studies on the Talbot effect for SPP using an impedance boundary condition approach [19]. Lately, Zhang *et al.* have for the first time observed experimentally complex plasmon Talbot pattern generated by periodic indentations on a metal film [20].

In this paper we present both experimental and theoretical study of the plasmonic Talbot effect generated near a periodic arrangement of nanostructures on a thin metal film. We develop a simple theoretical model based on a dipole scattering approximation taking into account a finite number of dipolar scatterers and describes the full physics involved. On the experimental side, we first study the Talbot effect using leakage radiation microscopy. We show that it is possible to create complex Talbot carpets using plasmonic fields after transmission or reflection from a periodic array of metal nanostructures lying on a metal film. Next we perform heterodyne interferometer based near-field microscopic characterization of the plasmonic Talbot pattern and reveal the phase and amplitude information of the Talbot carpet pattern. The subwavelength resolution of the near-field microscopic images enables us to measure the spatial confinement of individual Talbot hot-spots.

2. Theoretical description of the plasmonic Talbot pattern

The Talbot effect is usually described as a periodic self constructive focusing of light passing through a periodic structure. This effect is a direct consequence of the Fresnel diffraction that assumes that each element of the structure emits a spherical wave whose spatial dependence is proportional to e^{ikR}/R . The term e^{ikR} represents the propagation behavior, while the $(1/R)$ dependence allows the energy conservation flow through a surface surrounding the source of wave emission. The field measured at any position after the periodic structure is the sum of the field created by all the individual sources at this position. It is straightforward to deduce the expression of the Talbot length τ with such approximations. To model the plasmonic Talbot effect a similar hypothesis can be used. Nevertheless, applying Fresnel formula directly for plasmonic structures is not justified and Fourier optics for surface waves has to be considered in such cases [21]. Indeed, surface plasmons are two-dimensional waves and not spherical waves. As a result, the $(1/R)$ dependence, valid only in the three-dimensional case, does not hold anymore and has to be replaced by a $1/\sqrt{R}$ dependence [9]. Hence, the modeled field emitted by a single dipolar emitter is now proportional to:

$$G(\vec{R}) = \frac{e^{i\vec{k}_p \cdot \vec{R}}}{\sqrt{|\vec{R}|}}, \quad (1)$$

where $\vec{k}_p = 2\pi/\lambda_p$ is the wave vector of the plasmon whose real part gives the wavelength of propagation λ_p at the interface and imaginary part gives the damping due to Joule effect during propagation. Here \vec{R} is a vector in the interface plane, whose norm $|\vec{R}|$ gives the distance between the measured field and the dipole emitter position.

To calculate the field at any point of the interface, each emitter is assumed to have a dipolar moment p_n induced by the driven field such as $p_n = \alpha E(\vec{R}_n)$, where α represents the polarisability, \vec{R}_n the emitter position in the interface plane indexed by the integer n and $E(\vec{R}_n)$ the field at position \vec{R}_n . With those notations, the field $E(\vec{R})$ at any position \vec{R} satisfies the following expression:

$$E(\vec{R}) = E^{inc}(\vec{R}) + \sum_n G(\vec{R} - \vec{R}_n) p_n = E^{inc}(\vec{R}) + \alpha \sum_n G(\vec{R} - \vec{R}_n) E(\vec{R}_n). \quad (2)$$

The field measured at any position $\vec{R}, (\vec{R} \neq \vec{R}_n \forall n)$ is the sum of the incident field $E^{inc}(\vec{R})$ at position \vec{R} added by the contribution of the field of all the independent emitters. This expression is a reformulation of the Lippmann-Schwinger equation for this particular case. For $\vec{R} = \vec{R}_n$ the self interaction when $n = n'$ has to be removed from the sum over all the structures. Expression (2) becomes:

$$E(\vec{R}_n) = E^{inc}(\vec{R}) + \alpha \sum_{n \neq n'} G(\vec{R}_n - \vec{R}_{n'}) E(\vec{R}_{n'}). \quad (3)$$

By changing notations $E(\vec{R}_n) = E_n, G(\vec{R}_n - \vec{R}_{n'}) = G_{nn'}$ for $n \neq n'$ and 0 for $n = n'$ this self consistent equation can easily be casted into a matrix of the form

$$E = E^{inc} + G \cdot E, \quad (4)$$

where E is the column vector of elements E_n and G a square matrix of general term $G_{nn'}$. Note that the condition $G_{nn'} = 0$ for $n = n'$ allows removing naturally the self interaction between the structures themselves. By inverting (4), we end up with:

$$E = (Id - G)^{-1} \cdot E^{inc}, \quad (5)$$

where Id is the identity matrix. The column vector E represents the field at the dipole emitter position which is the result of the incident field and the cross interaction between the nano-emitters themselves. Deducing E by solving Eq. (5) and introducing the solution in Eq. (2) we are able to calculate the field at any position at the interface plan. The dimension of the matrix G is exactly the number of pillars. In accordance with our experimental samples, we consider only 20 nanostructures for the numerical simulations, which makes the equation solvable rapidly. Working with gold film at a wavelength around 785 nm, the damping of plasmon propagation can diminish the observation of the Talbot carpets. To permit all the dipole emitters to interfere efficiently, we kept the array parameters close to the wavelength. Moreover, this makes the Talbot pattern simpler for analysis.

Figure 1 (a) and (b) shows two examples of the plasmonic Talbot effect on a gold-air interface using our formalism for periods 800 nm and 1200 nm respectively. The images represent the intensity of the field for an area of $22 \mu\text{m} \times 22 \mu\text{m}$. The incident beam E^{inc} is a SPP having a transverse Gaussian profile $30 \mu\text{m}$ wide coming from the left to the right at a wavelength of 785 nm. We see clearly the incident beam being transmitted and reflected by the array forming a complex field pattern. This kind of plasmonic Talbot carpet has been already observed numerically by Dennis *et. al* [18] where the incident beam is launched perpendicular to the interface and not from the interface itself as in our case.

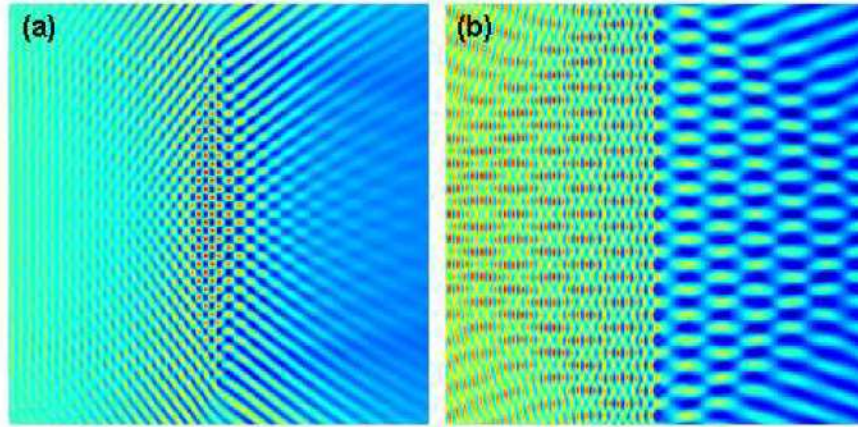


Fig. 1. Plasmonic Talbot-like distribution simulated numerically for an incident wavelength of 785 nm at periods (a) 800 nm and (b) 1200 nm. The SPP propagation direction is from left to right.

Interferences between the incident beam and the field reflected by the structure reveals an interesting Talbot pattern that exhibits a regular array of high contrast hot-spots close to the periodic structure. To estimate the Talbot length for the plasmon array structure from our simulations and the eventual deviation from the one given by the basic formula ($\tau = 2a^2 / \lambda$), we take the Fourier Transform of the intensity cross section perpendicular to the array axis. This way, we will immediately reveal eventual periodicities in the intensity field distribution.

Figure 2 shows the Fourier transform of intensity sections, i.e. the spatial frequency for an array period varying from 0.5 μm to 2 μm . The blue curve in Fig. 2 represents the Talbot lengths given by the paraxial approximation. Three main regions can be differentiated in the plot. An array period smaller than the wavelength (785 nm, shown as a vertical red dashed line) does not reveal any dominant periodicity. For an array period greater than twice the wavelength ($\approx 1.5 \mu\text{m}$), shown as a vertical green dashed line), we observe a perfect overlap of the paraxial approximation and our simulations. In between these two regions, the paraxial approximation drifts away from the calculation. Here the spatial frequency is larger than the one predicted which implies a shorter Talbot length than the one given by the formula.

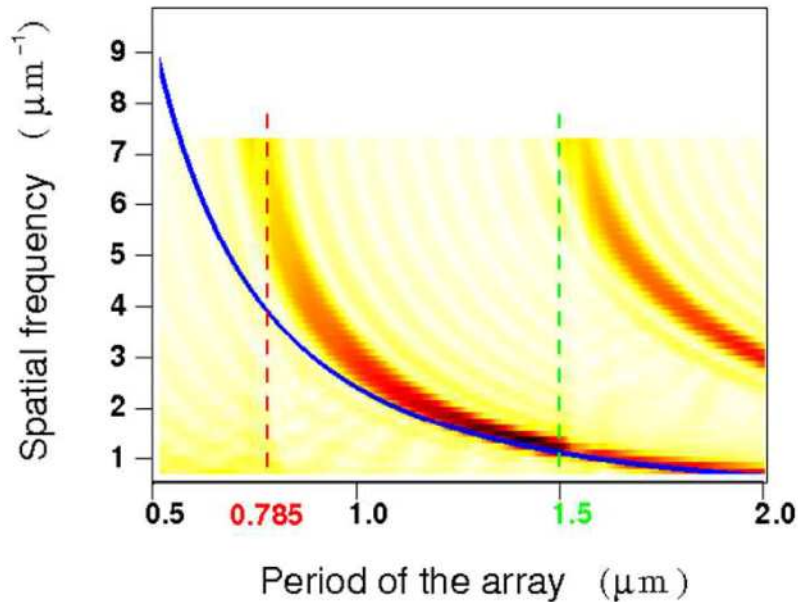


Fig. 2. Spatial frequency of the local intensity distribution as a function of the nanostructure period. The blue curve represents the Talbot distance for each period. The vertical red and green lines divide the plot into three regions.

Instead of adopting a rigorous model as in references [18] and [19], we chose to use a simple dipole scattering approximation to numerically simulate the plasmon Talbot-like effect. The formalism established here is purely scalar and does not take into account neither the vector nature of the electromagnetic field nor the tensor properties of polarisability α , nevertheless it allows to give us valuable information concerning the qualitative behavior of the plasmon Talbot effect.

3. Experiments and results

The sample, fabricated by electron beam lithography, consists of a row of cylindrical Au particles of diameter 200 nm and height 35 nm lying on a 50 nm thick gold film separated by a 20 nm thick SiO₂ layer. The spacer SiO₂ between the nanoparticles and the metallic film aims at reducing the direct quenching of the localized surface plasmons (LSP) resonance of the nanoparticles [22]. Two different periods (800 nm and 1200 nm) of the nanostructures were fabricated on the same sample to study the effect of the periodicity on the Talbot pattern.

3.1 Leakage radiation microscopic study

Leakage radiation microscopy is a far field technique that allows imaging the SPP propagation [23, 24]. In our set up SPPs are launched close to the structures using the Kretschmann-Raether configuration. This was done by illuminating light out of axis at a wavelength of 790 nm from a Ti:Sapph laser working in the CW-mode onto the sample through a high NA 60× TIRF objective. The image of leakage radiation is collected on a CCD after passing through a system of imaging optics.

The leakage radiation image captured by the CCD for two periods ($d = 800$ nm and 1200 nm) of the nanostructures is shown in Fig. 3. The incident SPP propagates towards the nanoparticle array from the left towards right. Part of the light is transmitted through the nanostructures while rest is reflected towards the incidence direction. The left side of the array shows high intensity regions due to the interference of the incident and the reflected

SPPs. The white dashed lines represent the approximate positions of the nanostructures. The near-field interaction of different diffraction orders creates a complex Talbot pattern close to the structures. A similar pattern is also observed in the reflection side of the structures. The Talbot pattern extends to several microns away from the nanostructures eventually fading away due to absorption in the metal. In the case of a array period close to the wavelength, the focal spots are sharp and well defined while for higher array periods (1200 nm) we observe broadened spots with low contrast. This qualitative remark can also be very well observed from the simulated images in Fig. 2.

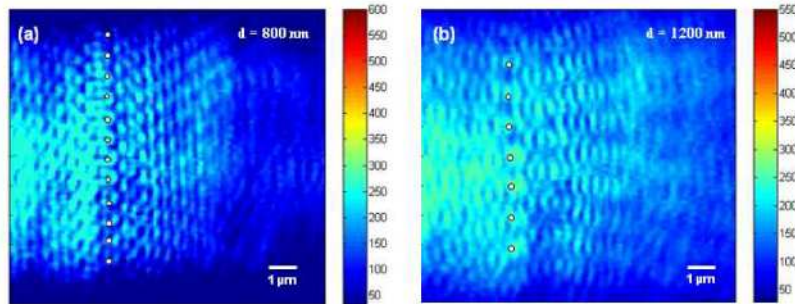


Fig. 3. Leakage radiation images of plasmonic Talbot carpets for two different periods. (a) 800 nm and (b) 1200 nm. The small circles in the images represent the approximate position of the nanostructures. The incident wavelength of light used in the experiment is 790 nm is incident from the left to right. Reflection of the SPP from the nanostructures creates high intensity regions which saturates the image on the reflection side.

For further analysis, an optical zoom of the leakage radiation image for the array period 800 nm is shown in Fig. 4(a). Several hot spots with a period equal to the array period are formed close to the nanostructures. This distribution of Talbot pattern forms an image of the array itself. We can also observe several orders or sub-images of the array at different positions of the image. The profile of the intensity across the image in the vicinity of the nanostructures is plotted in Fig. 4(b). The periodicity of the peaks from this profile is calculated to be 785 nm which is in good agreement with the separation (800 nm) between the structures. The small discrepancy between the values arises from the error of conversion from image pixels to real distance (micrometers) in the leakage radiation images.

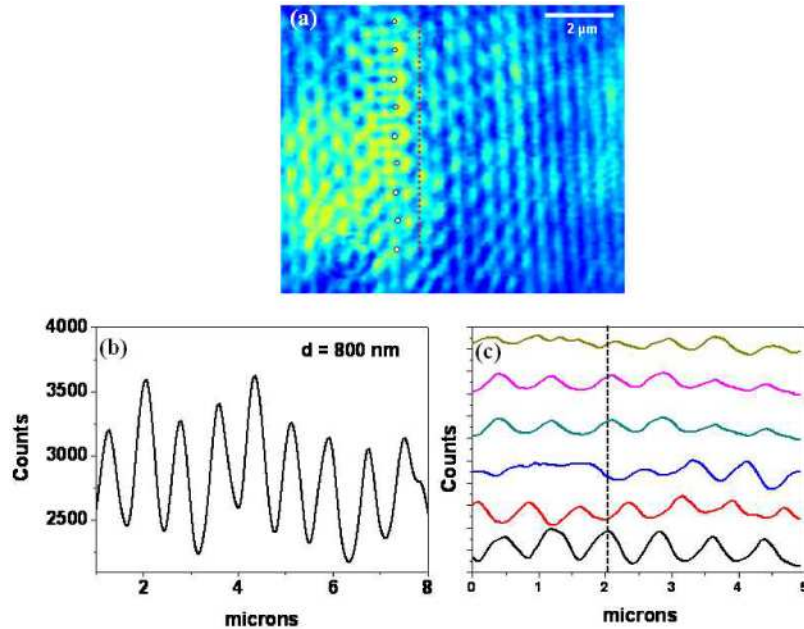


Fig. 4. (a) Optical zoom of leakage radiation image of plasmonic Talbot for a period of 800 nm. The small circles represents the approximate position of the nanostructures. (b) Intensity profile along the red dashed line in (a). The period of the intensity profile is calculated to be 785 nm, which is close to the actual separation of the nanostructures. (c) Evolution of the intensity hot-spots taken at consecutive rows close to the structures. We can observe the retrieval of the periodicity of the array at several locations in the image close to the nanostructures. The vertical dashed line in (c) is drawn along the peaks to show their spatial translations with respect to the first row.

In order to highlight the evolution of the reconstruction of the array's field at periodic distances in the Talbot pattern, we plot the intensity profiles across the image for the array period 800 nm for each vertical line of focal spots (Fig. 4(c)). One can also observe the 'spatially shifted' Talbot revival of the array pattern along with other fractional reconstructions arising from the interferences of the contributions from the nanostructures. It is interesting to observe here that there is a revival of the periodic focal spots that is repeated for several distances. Such kind of behavior is well observed in classical optics [25]. It should be noted here that the leakage images presented here contains only the intensity of the field and any phase change of the electric field is not recorded. In spite of being a diffraction-limited technique, leakage radiation microscopy provides valuable qualitative information on the distribution of the Talbot pattern.

3.2 Near-field amplitude and phase microscopy

The Talbot effect is usually depicted as a periodical self-focusing of the optical field after each Talbot length. More precisely, it deals with periodicity of the optical field intensity. Hence, it would be interesting to see the build-up of the Talbot effect by the phase development of the optical field throughout the Talbot length. To highlight this feature of the Talbot effect, information on the phase and amplitude of light are essential. We performed a heterodyne interferometer based near-field characterization of the plasmonic Talbot effect. In our setup, the incident SPP is launched by a standard Kretschmann configuration from a 785 nm laser diode. An uncoated optical fiber probe with a sub-wavelength apex size is used to pick up the light from the structure. The optical field is recorded while scanning over the sample. The fiber probe is kept in close proximity (~ 10 nm) to the surface by a shear-force feedback mechanism. In this proximity region, the local evanescent field tail of the light

propagating in the gold structure is coupled to the probe, converted into propagated waves, guided by the optical fiber and finally detected in the far field.

To retrieve direct information on amplitude and phase, a reference phase is needed. To this end the collected light is mixed with a reference beam into a heterodyne interferometer arrangement. This way, the interference between the two branches is obtained yielding both phase and amplitude of the local field [26–28].

Figure 5(a) shows an amplitude/phase measurement of a SPP launched towards a array of the nanostructures with a period of 1200 nm. The black circles represent pillars position as obtained from the shear force detection. We define the local optical field by the mathematical expression

$$E(x, y) = E_0(x, y) \cdot \exp[i\phi(x, y)], \quad (6)$$

where $E_0(x, y)$ is the amplitude and $\phi(x, y)$ the phase at position (x, y) . Figure 5(a) represents the map of the real part $E \cos(\phi)$ of the field obtained from the near-field experiment. We clearly observe the wave front of the incident SPP weakly diffracted by the array. The predominance of the incident plasmon makes the observation of any Talbot carpet difficult. Fortunately, having the optical field map in a complex form $E_0(x, y) \cdot \exp[i\phi(x, y)]$ allows us to analysis the Talbot effect in the Fourier space. Figure 5(b) shows the two dimensional FFT of the measured optical field in its complex form. The red circle in the image represents the light cone separating the lower spatial frequency wave vectors associated with scattered light into the free space and high frequency wave vectors associated with the evanescent waves bound to the surface (SPP). In order to reveal the presence of diffracted orders of SPPs by the array, we filter out most part of scattering into free space (gray region) as well as the incident SPP that dominates the spectrum. We can then clearly observe a series of orders of diffraction in the near field (bright spots indicated by a red arrow outside the light cone) and in the far field (bright spots inside the light cone). This implies that the array structures not only scatter light into plasmonic modes but into free space modes as well. Figure 5(c) shows the calculated real part of the optical field with the same parameters as used in our experiments

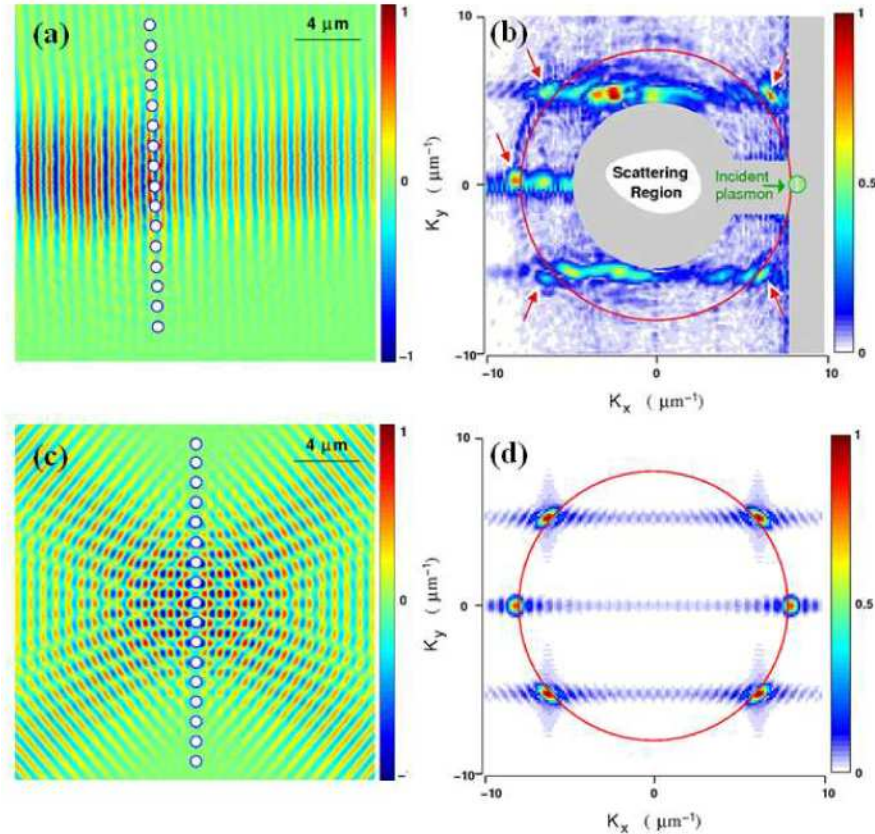


Fig. 5. (a) Observed near-field amplitude/phase image $E \cos(\phi)$ of the SPP propagation towards an array of the nanostructures with a period of 1200 nm. The black circles represent nanostructure positions as obtained from the shear force detection. (b) FFT of the complex optical field $E(x, y) = E_0(x, y)\exp[i\phi(x, y)]$ of (a). The red circle indicates the light cone. The central gray part depicts a filtering of the free space scattered light. (c) Simulated near-field amplitude/phase image $E \cos(\phi)$ corresponding to the parameters in (a). (d) FFT of the simulated optical field in (c).

To compare the calculations with our experimental result, we plot only the field created by the cylindrical nanostructures. The Talbot pattern is symmetric along the row of nanostructures which is a direct consequence of the assumption that the structures are point sources. Figure 5(d) is a two-dimensional Fourier transformation of the theoretically calculated optical field in Fig. 5 (c). We obtain a spectrum in very good agreement with the experimental one presented in Fig. 5(b). The diffraction spots are clearly outside the light cone (we did not take into account a free space coupling in the model) and are exactly at the same position as in Fig. 5(b).

To observe the Talbot effect in the direct space we need to eliminate the predominance of the incident plasmon. For this purpose, we make the reasonable assumption that wave vectors with a positive k_x represents the optical field forward scattered by the structures while the wave vectors with a negative k_x , represent the optical field, scattered in the backward direction by the structures.

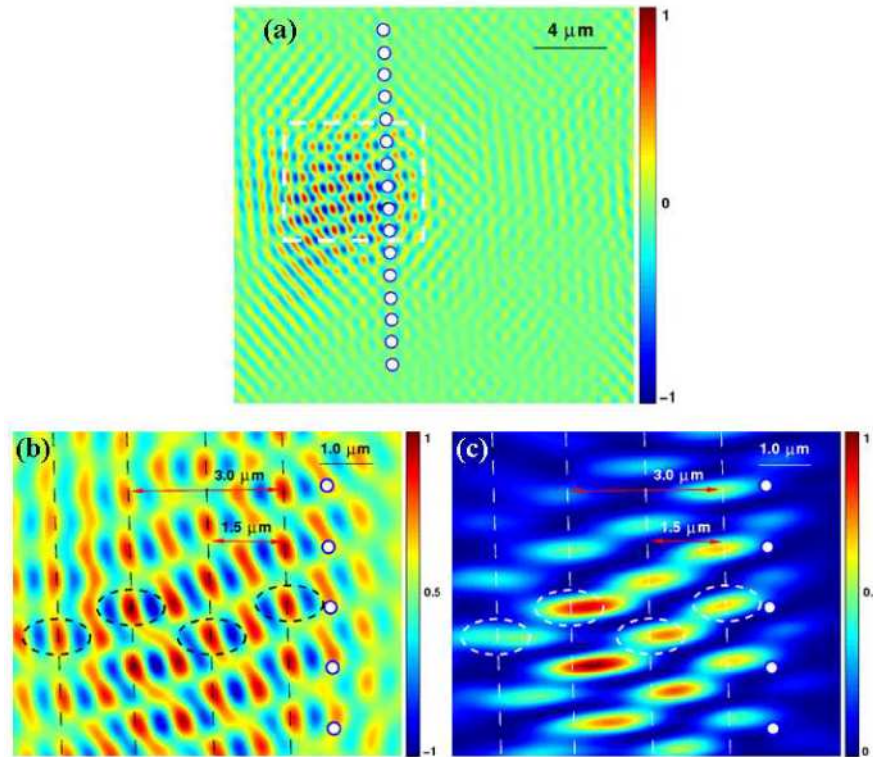


Fig. 6. (a) Optical near-field amplitude/phase image $E \cos(\phi)$ in Fig. 5(a) after filtering in the Fourier space. (b) Magnified image of the region inside the white square in (a). (c) Intensity image of the same region.

For the case of the incident plasmons having a positive wave vector, we can analyze the Talbot carpet in reflection instead of in transmission without having to lose information during the filtering process. Hence, keeping only negative wave vectors outside the light cone in our experimental data, we go back to the direct space performing an inverse fast Fourier transformation. We then apply a low pass filter and we get the real part of the optical field presented in Fig. 6(a). We can observe a very good agreement with the theory. Moreover, the field remains at the reflected side of the nanostructure array as predicted, proving that not only the relative position of the diffracted spots but also their shape and the relative phase in Fig. 5(b) are in good agreement with the theoretical one in Fig. 5(d). Figure 6(b) and (c) show the magnification of the central area. Figure 6(a) is the real part of the optical field and Fig. 6 (c) is its intensity. For a detailed analysis we identify a basic pattern in the region surrounded by the ellipses in Fig. 6(b). We observe a pattern of Talbot focal spots reproduced periodically separated by $3 \mu\text{m}$ and also a pattern that is laterally translated at half the Talbot length. We may recall that since we are dealing with the complex expression of the optical field, those periodicities at Talbot length and half Talbot length are actually periodicities in amplitude as well as in phase of the optical field. We can also observe that the optical field intensity pattern is slightly shifted with respect to the ellipse's position. This is a direct consequence of an additional phase accumulation during propagation away from the array. For this geometry, the Talbot length given by the paraxial approximation should be $3.7 \mu\text{m}$. Our evaluation of the Talbot length of $3.0 \mu\text{m}$ is in fair agreement with the calculation from the plot shown in Fig. 2 which predicts a shorter Talbot length for periods close to the wavelength.

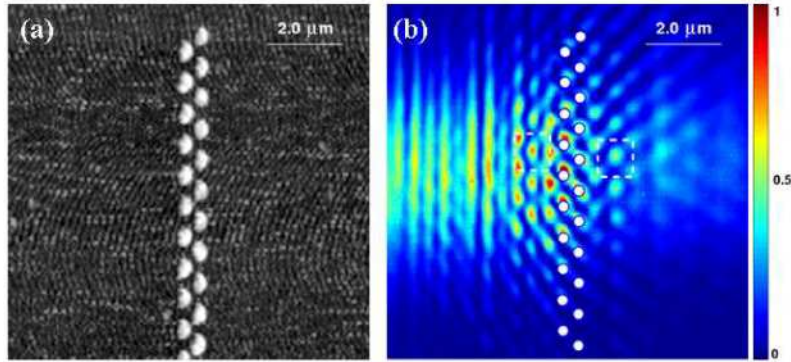


Fig. 7. (a) Shear-force image of the nanostructures. (b) Near-field intensity image of the field collected by the optical probe. The small white squares are regions of special interest. The structures have a period of 800 nm and separation between the rows is 400 nm.

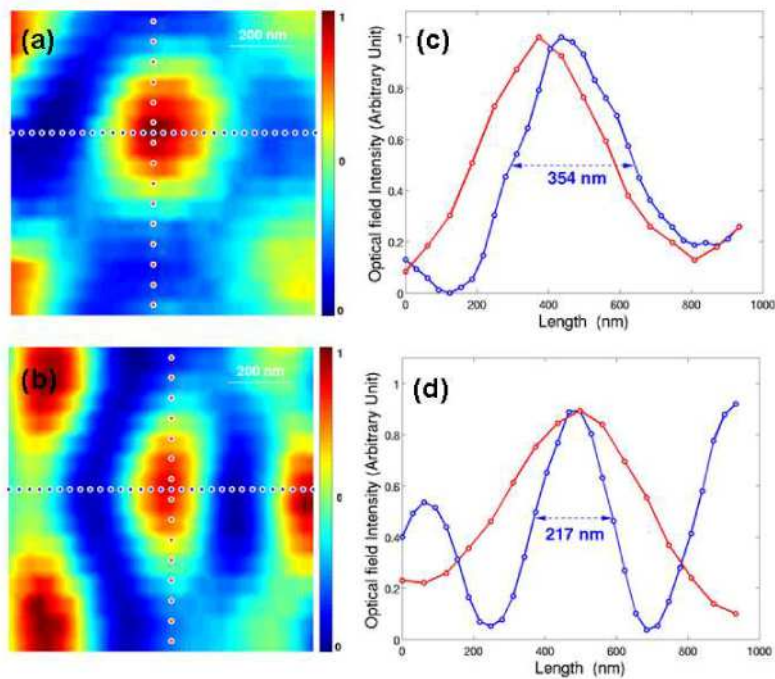


Fig. 8. (a) The Talbot hot-spot in the transmission side of the particle array. The red and blue circles represent the transversal and longitudinal directions. (b) Intensity profiles in the transverse (red) and longitudinal direction (blue). (c) The Talbot hot-spot in the reflection side of the particle array. (d) Intensity profiles in the transverse (red) and longitudinal direction (blue).

The Talbot intensity spots close to the nanostructures have well-defined features. This can be verified from both the theoretical plots as well as the near-field images. These hot-spots are narrower at positions where constructive interferences between the incident plasmon and the reflected field by the array occur. To measure experimentally the size of the spots, we made a near field intensity image of the propagation of the SPP through the 800 nm array. To increase the scattering cross section, we used double rows of the array separated by 400 nm from each other in the experiment. Figure 7(a) depicts the shear force image obtained

simultaneously with the optical signal. Figure 6(b) shows the intensity of the field collected by the optical probe. The nanostructure positions are represented by circles.

Figure 8(a) and (b) show the magnification of two regions where sharp contrast hot-spots have been located. One region is taken from the transmission side while the other from reflection part. To have a better estimation of the dimensions of each spot, we applied a linear interpolation on them. For the spot at the transmission side, the FWHM of the spot has been measured to be close to $\lambda/2$. On the other hand, the spot at the reflection side measures 217 nm longitudinally and 430 nm in the transverse direction. We can observe a ‘nano-focussing’ of the hot-spot in one direction with a FWHM close to $\lambda/4$ while a widening occurs in the other direction. It should be noted that these hot spots are more than one wavelength away from the nanostructures. This kind of asymmetrical behavior of the plasmon Talbot spots has been discussed theoretically by Dennis et al. [18]. Such localization of hot-spots could be of importance in nanolithography processes and optical sensing.

4. Conclusion

We have presented an experimental and theoretical study of the plasmonic Talbot effect. A simple theory based on a dipolar scattering is developed. Interesting patterns of hot-spots for a nanoparticle array period close to the wavelength are observed. The Talbot length calculated for such periodic array is shorter than that obtained from a paraxial approximation. Leakage radiation microscopy experiments were done to observe plasmonic Talbot effect. The leakage images of the plasmonic Talbot carpets obtained for periods of nanostructure array close to the wavelength give information on the complexity of the field patterns. Heterodyne interferometer based near-field measurement gives us an interpretation of the Talbot effect in the spatial Fourier space in terms of order of diffraction outside the light cone in perfect agreement with our simulations. The observed deviation from the Talbot length formula is in good agreement with theory. Plasmonic hot-spots of lateral dimension close to $\lambda/4$ have been observed. Such highly confined focal spots can find interesting applications in nanoscale plasmonic devices.

Acknowledgment

This research has been funded by the Spanish Ministry of Science and Innovation through Grant Nos. TEC2007-60186/MIC, CSD2007-046-NanoLight.es, the Juan de la Cierva program (D.H.) and by La Fundació CELLEX Barcelona. The authors would like to also acknowledge Jan Renger for his help in the leakage radiation microscopy experiment and Alberto G. Curto for fruitful discussions. SC and DH contributed equally to this paper.